Journal of Materials Chemistry A

ROYAL SOCIETY OF CHEMISTRY

PAPER

View Article Online
View Journal

Cite this: DOI: 10.1039/d6ta01878e

Mixed-dimensional multi-walled carbon nanotubes as a conductive network for improved lithium-ion battery performance

Ali J. Saadun,†[a] Steven D. Lacey, †[b] Yuri Surace, [c] Irshad Mohammad, [c] Karin Jägle,[d] Ivan Trentin,[d] Antonino Curcio,[a] Aliki Moysiadou,[a] Edouard Quérel, [a] Francesco Bizzotto,[a] Carlota Bozal Ginesta,[a] Peter Axmann, [d] Corsin Battaglia, [aefg] Florian Klunker[b] and Ruben-Simon Kühnel *[a]

Alternative conductive additives for lithium-ion batteries, such as carbon nanotubes and graphene, are academically well-established with pursued industrial opportunities while carbon black represents the global standard. However, further advancements are necessary to improve battery performance beyond current industrial metrics. Herein, a mixed-dimensional carbon material is introduced, featuring a network of 1D multi-walled nanotubes with 2D sheetlets, synthesized through a cost-effective process separating methane – a potent greenhouse gas – into carbon and low carbon intensity hydrogen. With proper slurry mixing, this material forms an expansive 3D conductive network within the electrode, enhancing electrical transport and thermal conductivity compared to carbon black electrodes. With only one-third of the carbon content (1 wt%), the electrical conductivity of a $LiNi_{0.5}Mn_{0.3}Co_{0.2}O_2$ cathode is 13 times higher than a carbon black reference, increasing both energy density and rate performance. The thermal conductivity is further improved by 40% (through-plane) and 200% (in-plane), promoting better heat dissipation. This carbon network also effectively retains transition metals during electrochemical cycling, limiting their migration to the anode, and thus reducing overall impedance build-up. The excellent compatibility of this conductive additive with state-of-the-art nickel-rich (85% nickel) layered oxides is also demonstrated, where 11.5 Ah pouch cells display >88% capacity retention after 1000 cycles at C/3.

Received 3rd March 2026
Accepted 9th June 2026

DOI: 10.1039/d6ta01878e

rsc.li/materials-a

1 Introduction

Evolving markets for mobile applications such as electric mobility and portable electronics continuously push lithium-ion battery manufacturers to meet ever higher performance metrics, particularly fast-charging capabilities and higher energy densities, where material developments are key.[1] Whereas a significant research focus is on developing high-capacity and high-voltage active materials,[2–5] an alternative strategy is replacing and reducing the content of inactive materials. On the cell level, this approach includes thinner and lighter current collectors,[6,7] reduced amounts of both conductive additives and binders in the negative and positive electrode,[8,9] as well as innovations regarding cell housing.[10]

Focusing on the development of conductive additives for the electrodes, a well-established material for lithium-ion batteries is carbon black (CB), which can be seen as the industry's standard.[8] However, the use of advanced carbon nanomaterials, such as two-dimensional (2D) graphene and 1D carbon nanotubes (CNTs), has gained significant attention in academia and industry due to their enhanced electrical, thermal, and mechanical properties.[8,11,12] A key advantage of such materials is that much lower carbon contents are needed compared to carbon black. Hence, energy density can be increased by replacing carbon black with 1D or 2D carbon materials. Another advantage is that their high electrical conductivity can improve rate performance. There are important differences between graphene and CNTs as a conductive additive for battery electrodes. While both classes of materials offer high thermal and electrical conductivity, large graphene sheets have been shown to block lithium-ion transport, thus negating the benefit of improved electronic conductivity at high rates.[13] On the other

[a]Empa – Swiss Federal Laboratories for Materials Science and Technology, 8600 Dübendorf, Switzerland. E-mail: ruben-simon.kuehnel@empa.ch
[b]Huntsman Advanced Materials GmbH, 4057 Basel, Switzerland
[c]AIT Austrian Institute of Technology GmbH, Center for Transport Technologies, Battery Technologies, 1210 Vienna, Austria
[d]ZSW Center for Solar Energy and Hydrogen Research Baden-Württemberg, 89081 Ulm, Germany
[e]ETH Zurich, Department of Information Technology and Electrical Engineering, 8092 Zurich, Switzerland
[f]ETH Zurich, Department of Materials, 8093 Zurich, Switzerland
[g]EPFL, School of Engineering, Institute of Materials, 1015 Lausanne, Switzerland
† Equal contribution.

hand, graphene has been reported to be particularly suitable for silicon-based electrodes by accommodating the volume change of silicon upon lithiation/delithiation.[14]

There are only a few reports on combining 1D and 2D carbon materials as the conductive additive. For example, Gao *et al.*[15] prepared a composite material by mixing silicon particles, graphene (reduced graphene oxide), and CNTs. The much-improved cycling stability compared to an electrode only with carbon black as conductive additive was attributed to a synergistic effect of the two different carbon nanomaterials. Ye *et al.*[16] combined carbon black, CNTs, and graphene in a graphite anode and attributed the improved cycling stability in part to a more effective solid-electrolyte interphase (SEI) forming in the presence of this multidimensional conducting network. Xue *et al.*[17] obtained better rate performance and cycling stability of $LiCoO_2$ cathodes containing three different carbons (*i.e.*, carbon black, CNTs, and graphene) compared to an electrode containing only carbon black but in a 50% higher content.

This work investigates a novel mixed-dimensional carbon nanotube material, composed of interconnected 1D tubules that can unfold into an intricate 3D network of 2D sheetlets, as a conductive additive for $LiNi_xMn_yCo_zO_2$ (NMC)-based cathodes. Slurries of this carbon nanotube network (CNT-N) material can be integrated seamlessly into conventional electrode manufacturing protocols and enhance overall electrode properties *versus* the reference carbon black cathode. Both the intrinsic material and electrode properties are quantified and their effect on battery performance is evaluated herein by electrical, thermal, mechanical, rheological, and electrochemical means. It is proposed that the combination of 1D and 2D material properties enables higher electrical and thermal conductivities of the resulting cathode coating, thereby positively influencing the overall cell performance, including higher capacity and enhanced rate capability. The results for CNT-N are compared to those obtained for conventional C65 carbon black as well as KS6L graphite.

2 Results and discussion

2.1 Carbon morphology effects on thermal- and electrical conductivity

Typical preparation procedures for the multi-walled carbon nanotube network (referred to as CNT-N), carbon black, and synthetic graphite are presented in Fig. S1. Carbon black is usually derived from high-temperature decomposition of petroleum products in an oxygen-poor atmosphere, whereas the common preparation method for synthetic graphite involves subjecting unstructured carbon, such as petroleum coke, to high temperatures (>2500 °C).[18,19] In contrast, the CNT-N material is produced by methane pyrolysis, where methane (CH_4) is converted into a structural carbon with hydrogen gas as another valuable byproduct. In principle, the methane feedstock for this process can also be sourced from flare gas or renewable natural gas (biomethane).[20,21] Due to the preparation procedure, CNT-N exhibits a mixed-dimensional structure composed of interconnected 1D multi-walled carbon nanotubes and 2D sheetlets (Fig. 1a and S2). The CNTs in CNT-N have typical diameters of >5 nm and lengths of up to 1.3 mm, with average lengths in the hundreds of microns range. To the best of our knowledge, this is a unique material that combines the properties of CNTs and graphene in terms of thermal and electrical conductivity as well as the ability to wrap around and cover active material particles, which has important benefits as discussed below.

For comparison, commonly used battery-grade C65 was used as a representative standard for the family of carbon black materials while KS6L graphite was also included in this study. SEM images confirm the sphere-like agglomerations of C65, whereas KS6L exhibits irregularly-shaped flakes (Fig. 1a). The BET surface area of the carbon materials are 18.6, 64.9, and 119 $m^2\ g^{-1}$ for KS6L, C65, and CNT-N, respectively (Table 1). Whereas the surface area of CNT-N surpasses that of C65 by nearly two times, its pore volume is only about 1.6 times larger (Table 1). The low pore volume value of KS6L indicates that the majority of the flakes have minimal accessible porosity. The Raman spectrum of the CNT-N material is shown in Fig. S3. The low D-band-to-G-band intensity ratio indicates a low defect density and a high degree of graphitic ordering of the CNTs.

To investigate the conductive properties of a standard cathode coating, a slurry with a NMC : PVDF : carbon weight ratio of $97 - x : 3 : x$ was prepared. For reliable comparisons, the PVDF content of all cathode slurries was kept constant to eliminate influences impacting the electrode's conductivity. Herein, dry powders of C65 and KS6L were processed directly into a uniform cathode slurry through centrifugal mixing, whereas CNT-N was prepared separately into a dispersion by high-shear mixing in order to homogenously distribute it in a PVDF/NMP solution beforehand. In general, dispersing CNTs can be a challenging task requiring careful optimization of surfactants, dispersants, or other polymeric additives to ensure the individualized tubes remain separated and stable in solution.[22] Hence, the dry CNT-N was processed in the PVDF/NMP solution with an additional polymeric material (distinct from PVDF) as a dispersant to sufficiently disperse the nanotube network and reduce agglomeration. The resulting CNT-N dispersion was subsequently combined with NMC and further homogenized during electrode slurry preparation. The dispersant remains in the electrode after drying and is therefore part of the inactive component fraction. A CNT-N-to-dispersant ratio of 10 : 3 was chosen to enable dispersions with sufficient long-term storage stability. The dispersion process also aids in unfurling some tubules into 2D sheetlets with dimensions on the order of tens of microns, which wrap around the active NMC particles when prepared into a cathode slurry. Specifically, we found that mixing the active material with the CNT-N dispersion before adding the remaining PVDF and NMP amounts (if needed) promotes the desired wrapping of CNT-N sheetlets around the active-material particles.

As expected, slurries containing CNT-N exhibit significantly higher viscosities than slurries containing C65 at the same carbon content. Fortunately, the required amount of CNT-N is substantially lower than that of C65, as indicated by the electrical and thermal conductivity data in Fig. 1c and d and by the electrochemical data presented below. Fig. S4 summarizes the

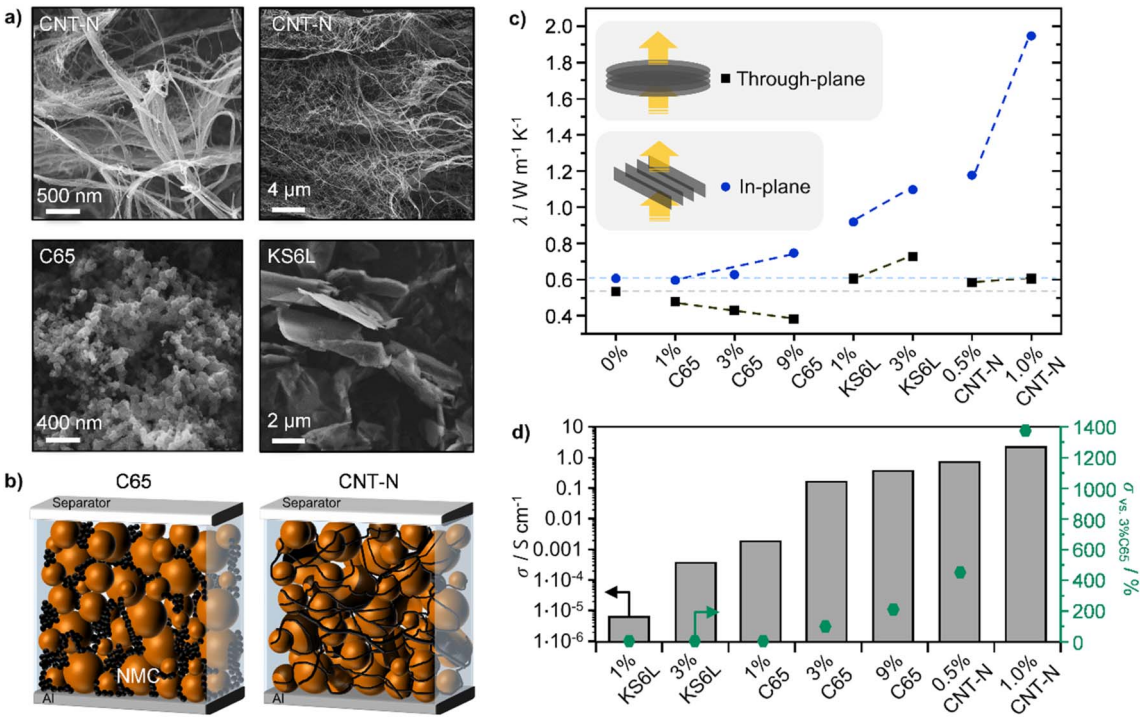

Fig. 1 SEM images of (a) the multi-walled carbon nanotube network (CNT-N), C65, and KS6L, and (b) a schematic illustration of an NMC cathode containing C65 or CNT-N, where the latter showcases both CNT tubules bridging between active NMC particles while some NMC particles are wrapped with 2D sheetlets (*i.e.*, unfurled CNT bundles). The measured (c) thermal conductivity in different configurations (through- and in-plane) and (d) electrical conductivity of the cathodes containing the three carbon types with varying weight loading. Note that the thermal conductivity was calculated from the measured thermal diffusivity of the samples.

Table 1 Measured surface area, pore volume, and specific heat capacity of battery materials

Material	Surface area S_{BET} [a] ($m^2\ g^{-1}$)	Pore volume V_{pore} [b] ($cm^3\ g^{-1}$)	Specific heat capacity c_p [c] ($J\ g^{-1}\ K^{-1}$)
C65	64.9	0.27	0.69
CNT-N	119	0.43	0.72
KS6L	18.6	0.07	0.59
NMC532	0.3	0.001	1.04
Al foil	—	—	0.96
Cu foil	—	—	0.42
Cathode with 3% C65	—	—	1.07
Cathode with 1% CNT-N	—	—	0.97
Graphite anode	—	—	0.60

[a] BET model. [b] Volume of N_2 adsorbed at $p/p_0 = 0.98$. [c] DSC measured at 293 K and calculated with the c_p-ratio method, using sapphire as reference material.

rheological data of the NMC slurries investigated in this study, all prepared with the same PVDF binder content (3 wt%) unless stated otherwise. Note that, in all cases, the viscosities were sufficient to cast the slurries onto Al foil. At 1 wt% CNT-N, the viscosity remains up to one order of magnitude higher over the investigated shear-rate range compared to a slurry with 3 wt% C65 (both containing 3 wt% PVDF binder). When the CNT-N content is reduced to 0.5 wt% while keeping the binder content at 3 wt%—a CNT-N level that is sufficient based on the electrochemical data presented below—the viscosity difference decreases markedly. When the binder content is further reduced to 1.5 wt%, the resulting slurry exhibits a lower viscosity than the slurry containing 3 wt% C65 and 3 wt% binder, particularly at high shear rates. Thus, by tuning the slurry composition, the desired viscosity can be achieved with CNT-N while retaining high electrical and thermal conductivity.

Beyond slurry rheology, the casting process is another critical factor for the resulting electrode properties, such as thermal conductivity. In this process, the alignment of large-aspect-ratio materials like CNTs is more significantly affected by the casting direction than that of spherical carbon black particles (not considering the shape of carbon black agglomerates) (Fig. 1b).

To evaluate the effect of directionality on thermal conductivity, electrodes designated for laser flash analysis (LFA) were

carefully fabricated by casting the slurry in a single direction followed by precisely stacking the dried electrode cutouts to ensure alignment in either the parallel (in-plane) or perpendicular (through-plane) direction (Fig. S5). Importantly, these measurements were performed on free-standing electrodes without a current collector, thereby reflecting the intrinsic conductivity of the cathode coatings.

The LFA technique measures the time required for the opposite side of the sample to register a temperature increase upon exposure to laser pulses. The output is the thermal diffusivity α (in $mm^2\ s^{-1}$), which is aligned with the test sample's orientation. Multiplying the diffusivity by the volumetric heat capacity (density $\times$ specific heat capacity, $\rho\ c_p$ in J $m^{-3}\ K^{-1}$) gives the thermal conductivity λ (in W $m^{-1}\ K^{-1}$). The density across all samples was maintained at *ca.* 3.0 g cm^{-3} to ensure comparability, and the specific heat capacity was assumed to be constant at 1 J $g^{-1}\ K^{-1}$, reflecting the specific heat capacity of the dominant NMC component and is in good agreement with values measured for two select cathodes (Table 1).

Thermal conductivity measurements reveal distinct enhancements for CNT-N cathodes compared to those with graphite and carbon black, with pronounced differences between the in-plane and through-plane directions (Fig. 1c).

2.1.1 In-plane configuration. CNT-N demonstrates a 200% improvement for in-plane thermal conductivity compared to the conductive additive-free cathode (0%). On the other hand, low C65 loadings (1 and 3%) exert virtually no effect on the in-plane conductivity when compared to the 0% cathode. Only a high amount of 9 wt% C65 provides modest improvements in thermal conductivity, which is likely due to the formation of effective lateral networks along the plane of the electrode (coating direction) that bridge neighboring NMC particles. The KS6L graphite cathode achieves a high in-plane thermal conductivity owing to the high intrinsic thermal conductivity of graphite in the basal plane ($\sim$2000 W $m^{-1}\ K^{-1}$ for large perfect crystals)[23] and some preferential orientation of the graphite flakes along the coating direction. However, its performance is not superior to that with CNT-N. The overall thermal conductivity in the KS6L cathode is influenced by factors such as suboptimal contact between the graphite flakes, variations in flake size and orientation, and the quality of inter-flake contacts. These can compromise the formation of an ideal thermal network, thereby preventing KS6L from surpassing the performance of the CNT-N cathode in the in-plane direction.

2.1.2 Through-plane configuration. In the through-plane direction (perpendicular to the coating direction), the 1% KS6L cathode exhibits comparable thermal conductivity to 0.5% and 1% CNT-N cathodes (*ca.* 0.6 W $m^{-1}\ K^{-1}$) while a 40% improvement is apparent compared to the 3% C65 cathode. Notably, a reduction in thermal conductivity is observed at increasing C65 weight loadings. This unexpected decline might be related to an unfavorable rearrangement of the carbon black in the electrode during the calandering stage. Due to the higher weight fractions of carbon, having a lower intrinsic density than NMC, a higher pressure had to be applied during calandering to achieve a similar volume averaged density as for the other samples.

In summary, these results underscore the anisotropy in thermal transport within the cathodes and highlight the capability of CNT-N to enhance heat conduction, particularly in the in-plane direction.

These improvements in thermal conductivity can be expected to mitigate thermal gradients within a cell, which have been shown to be detrimental for cycle life and are a key consideration in battery thermal management.[24,25] Previous experimental studies demonstrated that non-uniform temperature distributions accelerate battery degradation even when the average cell temperature is unchanged. Cloos and Wetzel showed for 20 Ah NMC–LMO/graphite pouch cells that both in-plane and through-plane temperature gradients lead to faster capacity loss compared to homogeneous thermal conditions, with through-plane gradients being more detrimental, especially at elevated average temperatures.[24] Similarly, long-term cycling studies by Cavalheiro *et al.* demonstrated that spatial temperature gradients inside pouch-cell stacks result in non-uniform and accelerated degradation, with regions exposed to higher local temperatures aging more rapidly.[25] As the core of large-format cells typically experiences higher temperatures than the outer regions during operation, especially at high charge and discharge rates, reducing internal thermal gradients through improved electrode thermal conductivity is expected to benefit cycle life under otherwise comparable cell and operating conditions. Even when the total heat generation remains unchanged, enhanced heat spreading at the electrode level is expected to lower peak core temperatures, which can reduce the peak cooling power required to maintain cells within safe and durable operating limits.

To further investigate the conductivity metrics of the electrodes, a four-point probe was employed to measure the electrical conductivity of the cathodes. When 1% CNT-N is incorporated into an NMC cathode, a 13-fold increase in electrical conductivity is achieved relative to 3% C65 (Fig. 1d, right axis). Even at a modest 0.5% loading, CNT-N cathodes exhibit conductivity 4.5 times higher than that of 3% C65 cathodes. Overall, these trends are consistent with percolation behavior in composite electrodes, where electronic transport increases sharply once a continuous conductive network forms above a critical filler loading. For C65, the strong increase from 1% to 3% combined with the minimal additional improvement when increasing C65 further to 9% suggests that the effective percolation threshold in the NMC/PVDF composite is reached around a 3% loading. In contrast, CNT-N reaches substantially higher conductivity at 0.5–1% loading, indicating a lower effective percolation threshold and more efficient conductive-network formation, which we attribute to the high-aspect-ratio nanotube component and the mixed-dimensional morphology that facilitate particle bridging and long-range connectivity. Regardless of the carbon content, the electrical conductivity of cathodes containing KS6L graphite proves challenging. The flake-like structure of graphite likely hinders the formation of an uninterrupted flow path for electrons, a limitation that may also apply to the electrode with 1% C65, where the number of

carbon spheres may be insufficient to form a connected electrical network within the NMC cathode. Overall, CNT-N electrodes exhibit both enhanced heat- and electron transport within the positive electrode compared to the industry standard C65 based on the aforementioned thermal conductivity and electrical conductivity results, respectively.

2.2 Performance of NMC532 cathodes with 1 wt% CNT-N loading

To understand how conductivity metrics could impact electrochemical performance, half cells composed of NMC532 cathodes with either 3% KS6L, 3% C65, or 0.5 and 1% CNT-N were assembled and rate tested. The carbon content of 3% was chosen for the reference materials (KS6L and C65) based on the thermal and electrical conductivity of the resulting electrodes. Note that 3% is also widely considered a standard amount of conductive additive for such electrodes. SEM images of KS6L, C65, and CNT-N cathodes are shown in Fig. S6 and S7 and showcase the distribution of carbon and active materials. The carbon materials appear relatively well distributed in all cases. However, the KS6L particles are clearly too large to efficiently connect the NMC particles. Furthermore, it can be seen that CNT-N wraps thinly around NMC particles in a spider-web fashion (Fig. S6c). By cycling the half cells under various discharge conditions, the cathode performance can be evaluated. Here, we observe that 1% CNT-N electrodes display the highest capacity per NMC weight (Fig. S8) and per cathode coating weight (excluding the current collector) (Fig. 2) regardless of the applied charge or discharge rate while cathodes with KS6L graphite offer nearly zero discharge capacity starting from a discharge rate of C/5 (denoted in the plot as D/5). We attribute the poor performance with KS6L to the low electrical conductivity of cathodes with KS6L (see again Fig. 1d).

Expressing the dataset per cathode weight (Fig. 2) is more relevant for industrial applications, as it reflects energy density while accounting for variations in both NMC and carbon contents in the cathodes. This plot highlights another key advantage of CNT-N in that it requires less carbon within the electrode. Note that the PVDF binder content (3%) is maintained constant across all tested cathodes herein. However, for the 0.5% CNT-N cathode, the capacity falls below that of the 3% C65 cathode at discharge rates above 1C. This, along with surface area considerations, is a strong indication that a PVDF content of 3% may be excessive for the 0.5% CNT-N cathode, hindering kinetics, especially at high rates. Accordingly, the binder content for the 0.5% CNT-N cathode was reduced by half (1.5% PVDF) and the cathode was retested to assess the effect of PVDF on rate performance. On a per-cathode-weight basis, the 0.5% CNT-N cathode with 1.5% PVDF displays discharge capacities comparable to the 3% C65 cathode for a discharge rate of 3D, and higher capacity at all lower discharge rates (Fig. 2a). We expect that further optimization of the binder:carbon ratio is required to fully utilize the potential of CNT-N in industrially relevant NMC cathodes. For 3% C65 and 1% CNT-N, the discharge rate was increased beyond 3C to 10C

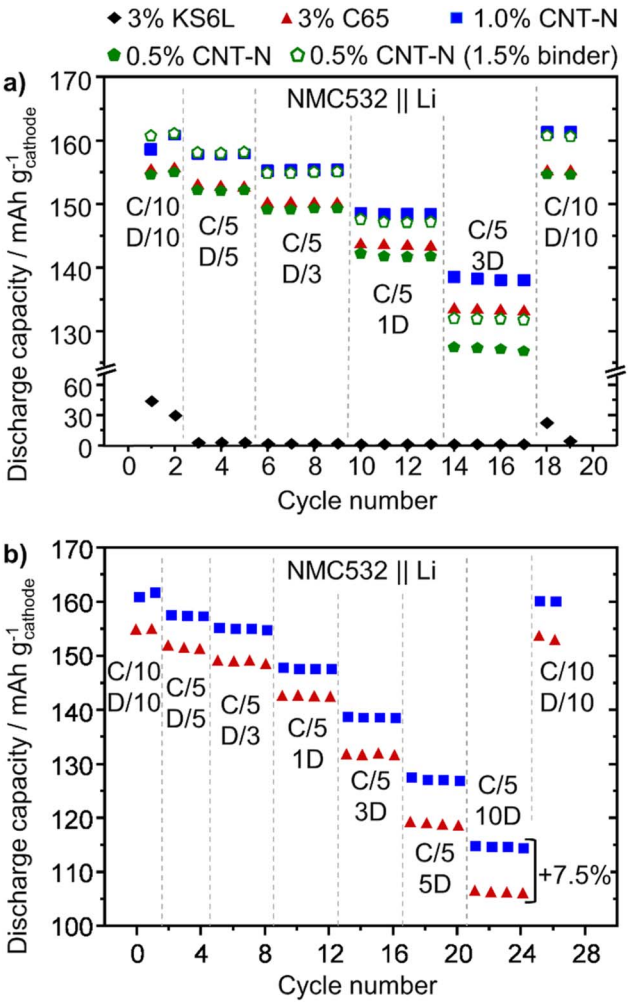

Fig. 2 Rate performance of Li‖NMC532 half cells at varying discharge (D) rates (a) from C/10 to 3C and (b) from C/10 to 10C. Unless otherwise stated, all cathodes have the same binder content of 3%. The cells were cycled at room temperature between 2.9 and 4.3 V. Electrolyte: 1 M $LiPF_6$ in EC : EMC 3 : 7 (by volume). All discharge capacities are reported per cathode weight without the current collector. Rate performance expressed per gram of NMC is shown in Fig. S8.

(Fig. 2b). At this very high discharge rate, the cell with 1% CNT-N delivers a 7.5% higher capacity per cathode weight.

In full cells, 1% CNT-N and 3% C65 cathodes were evaluated against standard graphite anodes (Fig. 3). At C/2 charge–discharge rates, 1% CNT-N cells rival the performance of those with conventional 3% C65, displaying a comparable capacity retention after 1000 cycles while the absolute discharge capacity is higher both per cathode and per NMC weights (Fig. 3a and b, S9). Note around cycle 400 a significant increase in discharge capacities is shown for all tested cells. During this time period, a temperature chamber malfunction caused the cell storage environment to increase by ~10 °C to ~35 °C. The 1% CNT-N cells also prove interesting for fast charging at 2C (with C/2 discharge), maintaining 74% of their initial capacity after 1000 cycles (Fig. 3a inset, Fig. 3c).

To estimate the benefit in terms of energy density for a realistic high-energy cell when switching from 3% C65 to 1% or

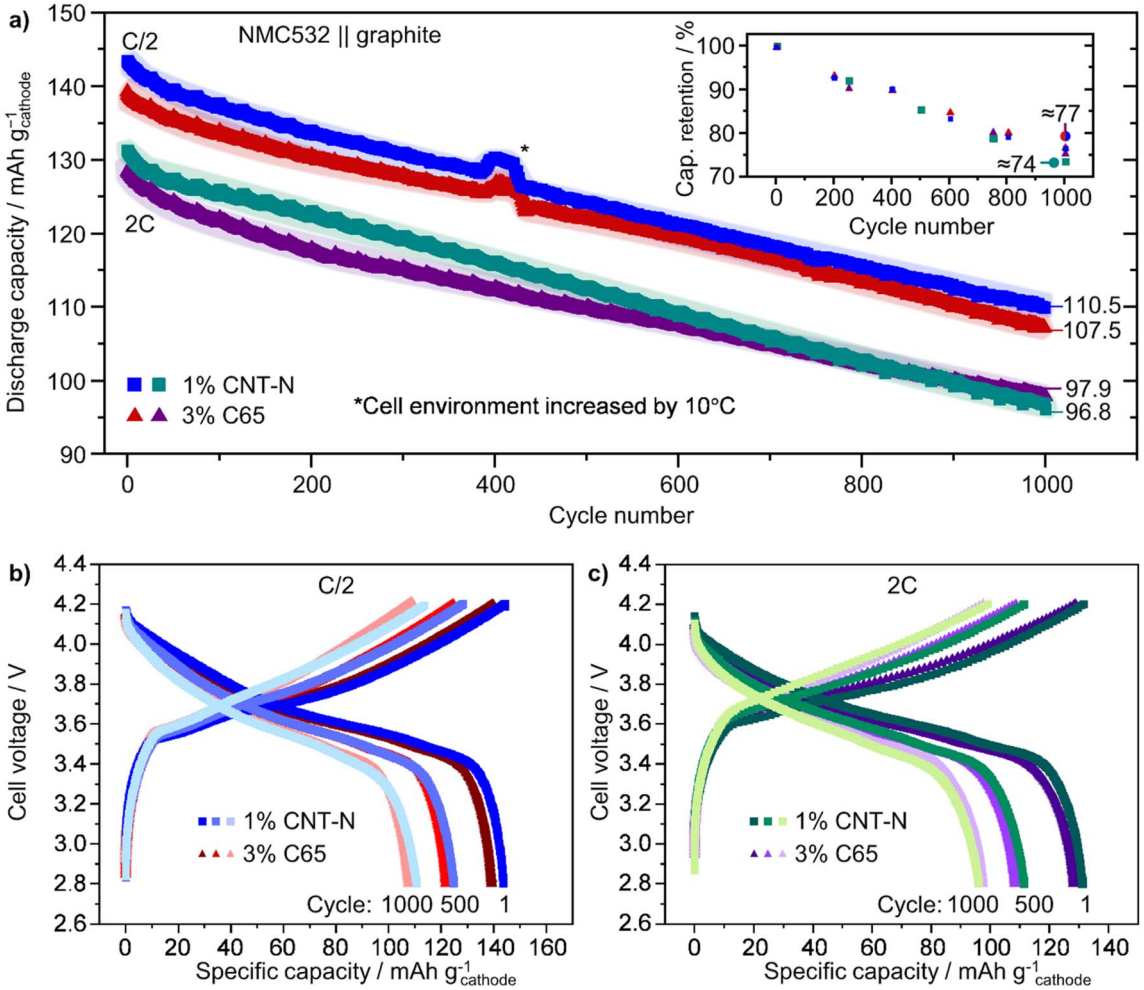

Fig. 3 (a) Long-term cycling stability including fast charging (top panel), and capacity retention (inset) of NMC532‖graphite full cells with 1 wt% CNT-N or 3 wt% C65 as conductive additive. The cells were cycled at room temperature between 2.8 and 4.2 V with a charge/discharge rate of C/2-D/2 or 2C-D/2 (1C = 170 mA g^{-1}); cell voltage profiles of cells cycled at (b) C/2 and (c) 2C. All discharge capacities are reported per cathode weight without the current collector. The shaded regions represent the deviation observed from testing 3 cells for each sample. N : P ratio: 1.2, electrolyte: 1 M $LiPF_6$ in EC : EMC 3 : 7 (by volume) + 2 wt% VC.

0.5% CNT-N, we assumed double-side-coated electrodes with an areal capacity of 5 mAh cm^{-2} per side, a gravimetric capacity of the cathode active material of 200 mAh g^{-1}, a binder content of 3%, and an aluminum current collector thickness of 10 μm. Under these assumptions, the gain in specific capacity on the electrode level is 2.1% when decreasing the conductive additive content from 3% to 1%. When further decreasing the CNT-N content to 0.5% and the binder content to 1.5%, the gain is 4%. These gains in specific capacity on the electrode level translate to gains in gravimetric energy density on the cell level of 0.8% and 1.6%, respectively, assuming a weight fraction of the cathode of 40%. Assuming no change in porosity, a gain in volumetric energy density on the cell level of *ca.* 1.5% and 2.5% can be expected for the 1% and 0.5% CNT-N cases, respectively, assuming a cathode volume fraction of 35%. To support this assumption, we performed a machine-learning-based porosity analysis on cross-sectional SEM images of fresh NMC532 electrodes containing either 1% CNT-N or 3% C65 and obtained similar porosity values for both formulations. Representative segmentation maps of the SEM images, distinguishing solid phases (active material, conductive additive, and binder where identifiable) from pore space, are provided in Fig. S10 and S11. These estimated gains in volumetric energy density are higher than the gravimetric ones as the carbon materials have less than half the density of NMC and are quite significant considering the high maturity of lithium-ion battery technology.

2.3 Characterization of cycled electrodes: reduced transition metal migration

To provide further insights into the electrochemical behavior of the C/2 charge–discharge full cells, EIS spectra recorded during cycles 1 to 1000 were analyzed (Fig. 4a and b, S12). For quantitative analysis, the equivalent circuit model shown in Fig. 4a was utilized. The spectra were recorded at 3.7 V, *i.e.*, at an intermediate state of charge where neither anode nor cathode are blocking for lithium ions. As shown in Fig. S12, the fits

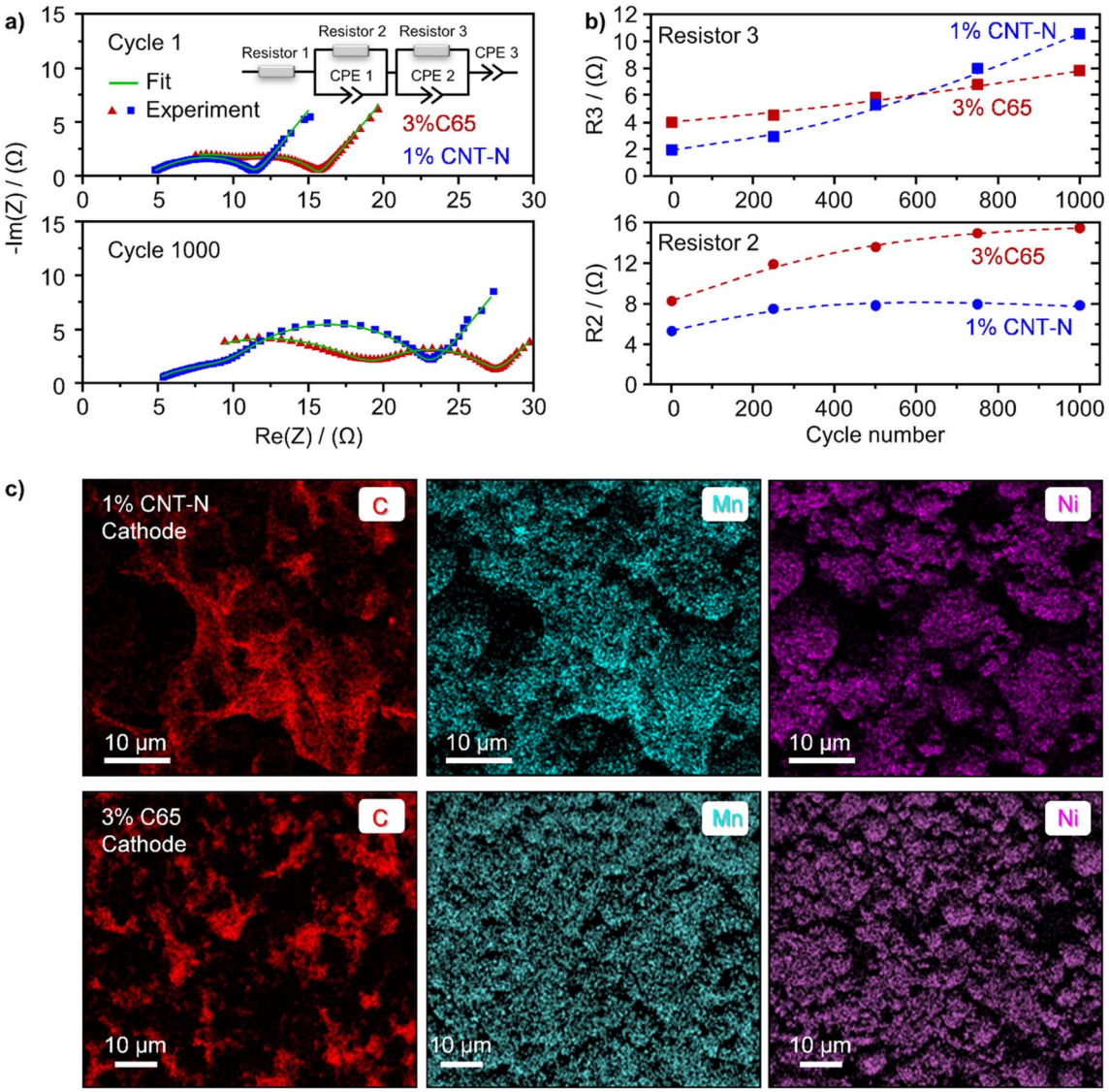

Fig. 4 (a) EIS spectra for the C65- and CNT-N-based cells recorded at 3.7 V at cycle 1 (after formation) and at cycle 1000. The equivalent circuit model used to fit the experimentally measured data is also shown in the figure. (b) Evolution of test cell resistance values over 1000 cycles. (c) EDX elemental maps of the 1000-times cycled cathodes containing 1% CNT-N and 3% C65. The cells were cycled at room temperature between 2.8 and 4.2 V with a charge/discharge rate of C/2 (1C = 170 mA g^{-1}). N : P ratio: 1.2, electrolyte: 1 M $LiPF_6$ in EC : EMC 3 : 7 (by volume) + 2 wt% VC. Additional EIS spectra can be found in Fig. S12.

using this model overlap with the measured data points quite well. The first semi-circle at high frequencies (represented by resistor 2 and constant-phase element (CPE) 1 in the model) is usually ascribed to the SEI on the anode and to a lesser extent to the passivation layer on the cathode. The second semi-circle at mid-frequencies (represented by resistor 3 and CPE 2 in the model; for the CNT-N cell only one semi-circle is visible for the first cycle) is commonly assigned to charge-transfer at the electrolyte/electrode interfaces.[26] As expected, both resistances tend to increase with cycle number. However, the passivation-layer resistance (resistor 2) does not increase further after 250 cycles for the CNT-N cell while it keeps increasing for the C65 cell (Fig. 4b). A possible explanation is that the CNT-N cathode limits the performance degradation of the graphite anode, considering that the SEI on the anode is usually the main contributor to the passivation-layer resistance of graphite/mid-nickel NMC cells. Taking into account that some of the NMC particles are covered by CNT-N in a spider-web fashion as discussed above, CNT-N could potentially suppress dissolution of transition metals from the cathode, which should lead to less electrolyte poisoning and growth of the SEI.

To further study the role of CNT-N on transition metal dissolution, post-mortem analyses of the cells cycled to 1000 cycles were performed including EDX (Fig. 4c), SEM (cross section and top view) (Fig. 5a), and ICP-OES (Fig. 5b). In the EDX maps for the cycled CNT-N cathode, signals from Mn and C overlap, highlighting again that CNT-N can wrap around NMC particles. In contrast, there is no clear overlapping pattern for

the C65 cathode as the C65 particles cover a smaller area of the NMC particle surface. The SEM images, particularly the cross-sectional images, show that the NMC particles are not damaged or cracked after 1000 cycles in either CNT-N or C65 cathodes. While we did not observe cracking for the NMC532 active material, we have no indication to expect that CNT-N significantly alters the cracking behavior of NMC materials with a high nickel content that are much more prone to cracking. We expect that the anisotropic strain due to volume changes upon lithiation/delithiation of such materials is not significantly altered by the presence of CNT-N due to the expected relatively flexible nature of the thin sheetlets. This indicates that the capacity fading shown in Fig. 3a is not a consequence of NMC particle cracking over prolonged cycling. In the top-view SEM images, the 'net' morphology of CNT-N is clearly visible, where the tubule bundles and 2D sheetlets wrap around the NMC particles forming a network (Fig. S13 and S14). Additionally, the graphite anodes recovered from the CNT-N and C65 cells after 1000 cycles were analyzed by ICP-OES to quantify the transition metal content (Fig. 5b). Importantly, the concentrations for all three tested transition metals, especially Mn and Ni, for the C65 anode far exceed the values for the anode from the CNT-N cell. Top-view SEM paired with EDX also showcases that Mn depositions are more pronounced on the cycled graphite anode surface for the C65 cell (Fig. S15). These findings suggests that the CNT-N within the cathode indeed suppresses transition metal dissolution. In literature, stabilization of NMC upon coating it prior with reduced graphene oxide has been beneficial and explained by the lower surface area of NMC that is in direct contact with the electrolyte.[27] Considering that the CNT-N does not fully cover the NMC particles in our case and hence electrolyte might still be able to reach some of the NMC surface, CNT-N might alternatively act as a kind of 'net' for dissolved transition metals, reducing its concentration in the electrolyte. A more detailed understanding of the mechanism of suppressed transition metal dissolution from NMC in the presence of CNT-N, particularly regarding the interaction between the electrolyte and the CNT-N-covered NMC particles, and to distinguish between the two proposed mechanisms, would be desirable and should be studied in future.

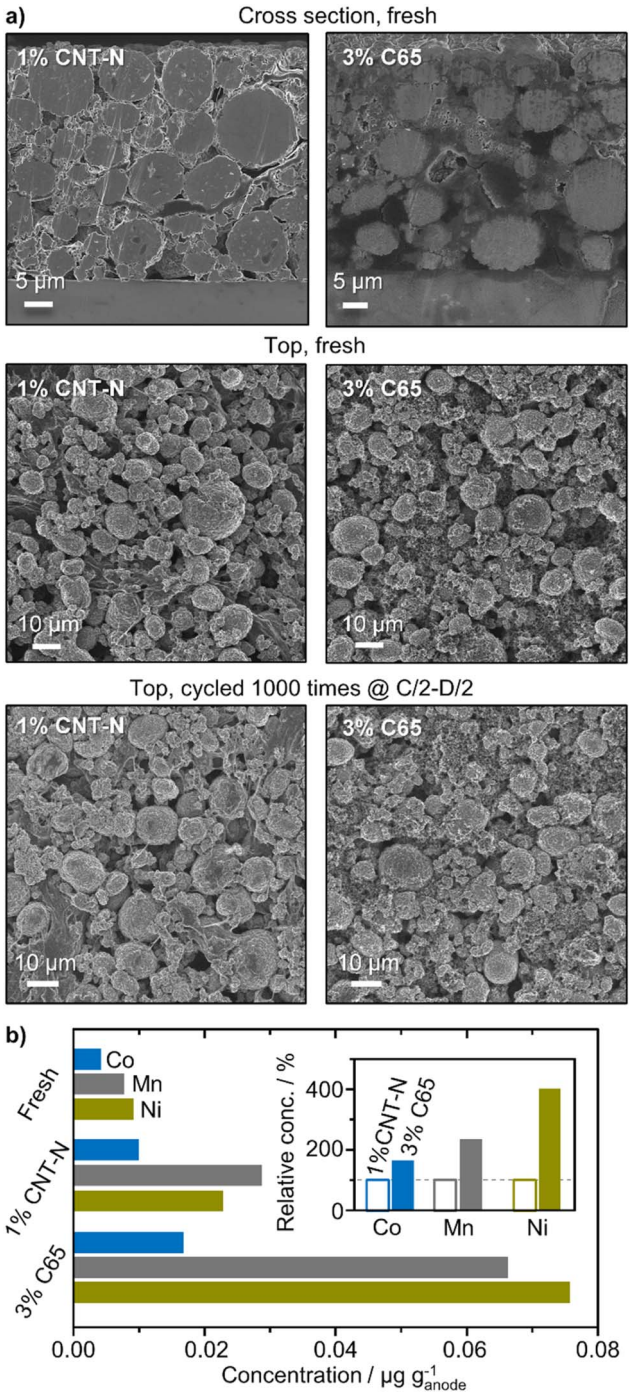

Fig. 5 (a) Cross-sectional and top-view SEM images of fresh and cycled cathodes and (b) transition metal concentration in the fresh and cycled anodes with the relative concentration in percentage displayed in the inset.

2.4 Nickel-rich NMC/graphite pouch cells with CNT-N

After the promising results with the mid-nickel NMC532 electrodes, nickel-rich $LiNi_{0.85}Mn_{0.07}Co_{0.08}O_2$ (NMC850708) cathodes were prepared using CNT-N as conductive additive and then assembled and cycled against standard graphite anodes in industrially relevant multilayer pouch cells. The cells contained 20 double-side coated graphite anode sheets and 19 double-side coated NMC850708 cathode sheets. The cathodes contained only 0.5% CNT-N as conductive additive and had a high active material content of 97.35%. The cells also featured a very high cathode loading of 5 mAh cm^{-2} and were subjected to constant current-constant voltage cycling at a rate of C/3 and two diagnostic cycles at C/10 every 100 cycles. The results of the cycling experiment are shown in Fig. 6.

After an initial drop in capacity of *ca.* 7% during the first 100 cycles, the cells display very stable capacity at C/3 as reflected in an average capacity retention around 88% after 1000 cycles, demonstrating excellent compatibility between CNT-N and Ni-rich NMC. Based on the decay rate over the last few hundred cycles, these multilayer NMC85/graphite pouch cells are expected to reach >1500 cycles before 80% capacity retention is

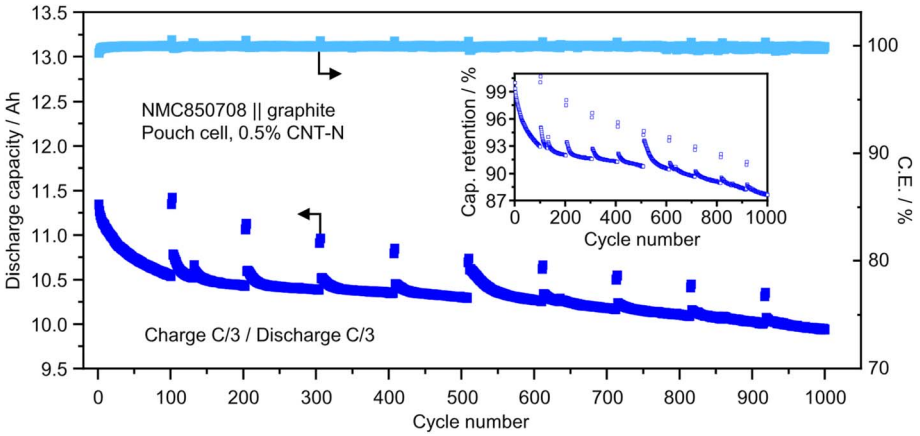

Fig. 6 Coulombic efficiency and long-term cycling stability of NMC850708‖graphite full pouch cells with 0.5 wt% CNT-N as cathode conductive additive. The cells were cycled at room temperature between 2.8-4.2 V with a charge/discharge rate of C/3 and two diagnostic cycles at C/10 every 100 cycles. All values are averages of two multilayer pouch cells. Electrolyte: 1 M $LiPF_6$ in EC : EMC 3 : 7 (by volume) + 2 wt% VC.

met, which surpasses the desired metric for industrial automotive batteries.[28]

In the broader literature on advanced conductive additives, performance gains are commonly reported for high-aspect-ratio 1D carbons (CNTs and carbon nanofibers) and multidimensional carbon blends because they reach percolation at low loadings. Carbon blacks, which typically require higher fractions, and 2D graphene-type platelets can introduce Li-ion transport limitations by obstructing pore pathways.[13,15–17] Against this backdrop, the electrical conductivity increase achieved here at only 0.5–1 wt% CNT-N (up to 13 times *vs.* 3 wt% C65) places CNT-N in the regime targeted by the CNT-based literature, while additionally quantifying a pronounced thermal-transport benefit (200% in-plane and 40% through-plane) that is rarely reported at the electrode level for such low additive loadings. Notably, prior work has shown that reduced graphene oxide and other coatings on NMC can mitigate degradation of the active material by reducing direct electrolyte contact area.[27,29] In contrast to these coating strategies, the reduced impedance build-up and suppressed transition-metal migration observed herein are achieved through a conductive additive introduced during slurry processing, suggesting that partial particle coverage and network formation can deliver interfacial stabilization without a dedicated active-material coating step. Overall, CNT-N therefore combines the low-loading percolation advantage typical of 1D carbons with an additional heat-management and aging-mitigation contribution that helps rationalize the improved rate capability and long-term stability observed in both coin and pouch cells.

3 Conclusion

In summary, the use of CNT-N as a cathode conductive additive promotes improvements on both the electrode and cell level. The unique carbon morphology of 1D tubules unfurling into 2D sheetlets allows this mixed-dimensional carbon material to wrap around active (NMC) materials and form an interconnected 3D conductive network within the battery electrode. Compared to the industrial standard carbon black (C65), CNT-N cathodes are 4.5–13 times more electrically conductive at 0.5–1.0% carbon contents than cathodes with 3% C65, which reduces cell resistance and leads to a more energy-dense cell from the increased active material content. CNT-N cathodes also display a 200% improvement in in-plane and 40% improvement in through-plane thermal conductivity while using a third of the carbon amount. These conductivity metrics likely lead to more efficient heat dissipation within larger cells, such as cylindrical or prismatic cells, which should be explored in future scale-up studies.

Moreover, excellent rate capability and long-term cycling stability is shown for mid-nickel NMC532 cathodes with CNT-N, reaching higher capacities per cathode weight and per NMC weight in half cells across all investigated C-rates as well as having similar capacity retention to C65 full cells after 1000 cycles at both C/2 and 2C charge rates. EIS and post-mortem analyses reveal a unique phenomenon enabled by CNT-N: suppression of transition metal dissolution into the electrolyte and hence less poisoning of the SEI. To the best of our knowledge, this is the first report of a conductive carbon additive that is added to the slurry and not coated on the active material that plays an active role in mitigating transition metal dissolution. Finally, CNT-N demonstrates excellent compatibility with nickel-rich NMC (85% Ni) cathodes, achieving a capacity retention of 88% in 11.5 Ah multilayer pouch cells after 1000 cycles at a C/3 rate, rendering it a promising solution for the automotive industry.

4 Experimental section

4.1 Electrode preparation

A schematic overview of the electrode preparation protocol together with the methods used for electrochemical testing and materials characterization is presented in Fig. S1.

4.1.1 Materials. Multi-walled carbon nanotubes (MIRALON® pulp, Huntsman Advanced Materials), hereafter CNT-N, carbon black (Super C65, Imerys), and graphite (KS6L, Imerys) were used as carbon conductive additives. Commercially available $LiNi_{0.5}Mn_{0.3}Co_{0.2}O_2$ (NMC532, D_{90} = 20.7 μm, Targray) was used as the active NMC cathode material for initial testing. High-shear mixing equipment was used to properly disperse the CNT-N in NMP solvent with PVDF (1 : 3 ratio of carbon : binder) and non-ionic surfactant/dispersant with loadings of 1.25 wt%, 3.75 wt%, and 0.375 wt%, respectively. An additional CNT-N dispersion with a higher carbon:binder ratio of 1 : 6, consisting of 0.5 wt% CNT-N, 3 wt% PVDF, and 0.15 wt% non-ionic surfactant/dispersant, was also available to ensure slurry preparation procedures were consistent across all evaluated carbons (carbon black and graphite). The CNT-N dispersions were supplied by Huntsman Advanced Materials and used directly to prepare cathode slurries.

4.1.2 Cathode preparations. Slurries containing C65 or KS6L as carbon additive were prepared by mixing the cathode active material and the carbon powder with polyvinylidene fluoride (PVDF, Solef® 5130, Solvay) in *N*-methyl-2-pyrrolidone (NMP, Sigma Aldrich, 99.5%) to achieve a ratio of NMC : PVDF : carbon of 94 : 3 : 3, unless otherwise indicated. The components were mixed in a centrifugal Thinky Are-250 mixer for 20 min at 2000 rpm followed by degassing for 5 min at 500 rpm. To create the CNT-N cathode slurries, NMC powder was added to the CNT-N dispersion and mixed in a Thinky mixer using an identical protocol as described above to achieve a homogeneous slurry with final NMC : PVDF : CNT-N : surfactant ratio of 95.7 : 3 : 1 : 0.3 or 96.35 : 3 : 0.5 : 0.15. Slurries with reduced PVDF binder content resulted in a final ratio of 97.85 : 1.5 : 0.5 : 0.15. All slurries contained a total solids content of 50% and were coated on an aluminum current collector using a Zehntner ZUA series film applicator. The wet electrodes were subsequently dried under air atmosphere at 80 °C for 30 min. The electrodes for the coin-cell experiments were precision cut into discs with a diameter of 15 mm (graphite anode) or 14 mm (cathode) using an EL-Cut (EL-Cell) punching tool and dried at 80 °C under vacuum for 15 h prior to cell assembly.

4.2 Materials characterization

4.2.1 Slurry. The rheological parameters including the viscosity and the shear rate of the slurries were measured on a TA Instruments AR 1500ex with a plate–plate geometry of 40 mm diameter, 0.1% strain, and gap of 0.5 mm. All rheological tests were performed at a temperature of 25 °C.

4.2.2 Thermal and electrical properties. Thermal diffusivity was measured using the laser flash technique on a Netzsch LFA 457 equipped with an infrared sensor to measure the temperature increase on the back surface of the sample. Sample preparation for in- and out-of-plane measurements of standalone electrodes is depicted in Fig. S5. An approximately constant density was maintained across the samples by calendering them under pressures ranging from 1 to 5 tonnes. The sample was placed in the holder and the chamber was evacuated and flushed with argon three times prior to the start of the measurement at room temperature. Differential scanning calorimetry (DSC) measurements were performed on a Netzsch STA 449 F3 Jupiter equipped with a liquid N_2 cooling system. The sample was placed in an Al crucible and pretreated in an N_2 atmosphere (10 cm^3 min^{-1}) at 25 °C for 1 h prior to controlled cooling to 223 K (5 °C min^{-1}). Upon stabilization of the temperature, the sample was heated up to 200 °C (5 °C min^{-1}); all in N_2 atmosphere. Empty reference Al crucibles were used to eliminate the influence of the crucible material on the measurement results whereas sapphire standards were utilized to aid in determining accurate specific heat capacity (c_p) values. The electrical conductivity of the electrodes was calculated from linear resistivity measurements performed with a four-point probe setup.

4.2.3 Morphology. Scanning electron microscopy (SEM) images were acquired using a Nova NanoSEM 230 FEI Field Emission SEM as well as LEO 1530 thermally assisted field emission SEM with energy-dispersive X-ray spectroscopy (EDS). Images were recorded using a variety of accelerating voltages (3–10 kV) and EDS spectra were collected using a 10 keV accelerating voltage. For cross-sectional SEM images, selected electrodes were ion-milled for 4 h at −70 °C to avoid the melting of organic components, using the broad Ar-ion beam of a Hitachi IM4000Plus.

N_2 sorption at 77 K was measured in a Micromeritics ASAP 2020 analyzer. Samples (approximately 0.10 g) were evacuated to 50 mbar at 100 °C for 12 h prior to the measurement. The Brunauer–Emmett–Teller (BET) method was applied to calculate the total surface area, S_{BET}. The pore volume, V_{pore}, was determined from the amount of N_2 adsorbed at a relative pressure of $p/p_0 = 0.98$.

4.2.4 Metal content. The metal loading in the anodes was determined by inductively coupled plasma optical emission spectroscopy (ICP–OES) using a Horiba Ultima 2 instrument equipped with photomultiplier tube detection. To ensure the dissolution of the metals, the full anode was cut in smaller pieces and placed in a vial containing 0.5 mL concentrated HCl (37%, Sigma Aldrich) and left for 12 h. An aliquot (0.2 mL) of this supernatant was taken and diluted in 9.8 mL 1.5% HCl prior to the measurement.

4.3 Battery experiments

The electrochemical performance of the coin cells was examined using 2032 type coin cells with two spacers (1 mm and 0.5 mm), a 1.4 mm spring, and a 16 mm Celgard 2500 series separator and were assembled in an Ar-filled glove box. The Li metal foil, used in half cells, was purchased from China Energy Lithium whereas the graphite anodes were obtained from CustomCells. 35 μL of 1 mol L^{-1} (1 M) $LiPF_6$ in ethylene carbonate (EC) and ethyl methyl carbonate (EMC) in a volume ratio of 3 : 7 with (full cells) or without (half cells) 2 wt% vinylene carbonate (VC) (Solvionic) was employed as electrolyte. Half cells were assembled using Li foil as counter electrode and cathodes with a typical areal active material loading of 8.0 mg cm^2 (areal capacity of 1.35 mA h cm^{-2}). For full cells, anodes and heavier cathodes with an areal capacity of 2.4 mA h cm^{-2}

and 2.0 mAh cm^{-2}, respectively, were used, leading to an N/P ratio of 1.2. After assembly of the full cells, the cells were charged to 1.5 V at C/3 to minimize corrosion of the Cu current collector, subsequently rested for 12 h to ensure wetting of separator and electrodes before starting constant-current charge–discharge tests. Charge/discharge full cell cycling data and electrochemical impedance (EIS) measurements were recorded on a BCS-805 (BioLogic), whereas a CT3001A (Wuhan LAND Electronic) battery cycler was used for the half cells.

All half- and full cells were cycled between 2.9–4.3 V and 2.8–4.2 V, respectively. Two formation cycles at C/10 followed by continuous charge and discharge cycling at C/2 was performed, if not otherwise stated. The full cells were subjected to constant current-constant voltage (CCCV) cycling. Full cells were also subjected to higher charge–discharge rates of 2C–C/2. Charging rates did not exceed 2C to alleviate dendrite growth in the cells. Unless otherwise stated, all electrochemical measurements were conducted at 25 °C.

Cycled cells were disassembled in the charged state inside an Ar-filled glove box. The positive electrode was recovered and thoroughly rinsed with EMC to remove electrolyte residues. Prior to post-mortem characterization, the electrode was maintained inside the glovebox for one hour to ensure the quantitative evaporation of the solvent.

The multilayer pouch cells were prepared in-house and consisted of 19 cathode and 20 anode layers. The cathodes had a composition of 97.35% W-coated NMC850708 (prepared in-house at ZSW), 0.5% CNT-N, 0.15% surfactant, and 2% PVdF (Solef 5130, Solvay). The anodes had a composition of 94% graphite (SPGT807, Targray), 1% carbon black (Super C45, Imerys), 1.5% carboxymethyl cellulose (Walocel CRT 30000 PA, Dow), and 3.5% styrene-butadiene rubber (Lipaton SB-5521, Synthomer). The cathode and anodes had a size of 68 × 98 mm^2 and 70 × 100 mm^2, respectively. All electrode sheets were coated double-sided. The cathodes and anodes had an areal capacity of 5.0 and 6.0 mAh cm^{-2}, respectively, resulting in an N/P ratio of 1.2. The areal capacity of the cathode is based on the reversible capacity of the NMC cathode material measured in a full coin cell with a graphite anode of 180 mAh g^{-1}. Further information about the pouch cells can be found in Table S1. Based on this information and the cathode loading, the calculated capacity of the cells is 5.0 mAh cm^{-2} × 6.8 cm × 9.8 cm × 19 × 2 = 12.7 Ah. Trilayer Celgard 2320 foil was used as separator. The electrolyte content of the cells was 3.2 mL Ah^{-1}. The electrolyte composition was 1 M $LiPF_6$ in EC : EMC 3 : 7 (by volume) + 2 wt% VC. The cells were degassed after two CCCV cycles of formation at C/20 and then subjected to long-term CCCV cycling at C/3 and two recovery cycles at C/10 every 100 cycles. The voltage range was set to 2.8 to 4.2 V and the cycling experiments were conducted at 25 °C using a Maccor S4000 battery test system.

4.4 Porosity estimation

The microstructural analysis was performed on cross-sectional SEM images. All images were processed using Python, employing libraries including OpenCV, NumPy, Matplotlib, and the Gaussian mixture modeling implementation from scikit-learn. A Gaussian Mixture Model (GMM) with $n = 10$ clusters was fitted to the pixel dataset, where each pixel is represented by a three-dimensional vector corresponding to the RGB color encoding. Each pixel was assigned to the most probable GMM cluster, resulting in a labeled segmentation map. To distinguish between material phases, the mean RGB intensity of each GMM cluster was computed and used as a proxy for contrast. Clusters were sorted according to their average intensity. A subset of clusters corresponding to lower brightness values was classified as the pore phase, while the remaining subset representing higher intensities was classified as the particle cross-section phase. This classification was adjusted empirically to balance sensitivity and robustness.

Porosity was estimated by computing the ratio of pixels assigned to the pore phase, N_{pore}, relative to the total number of pixels in both pore and cross-section phases, $N_{\text{pore}} + N_{\text{cross-section}}$:

$$\text{Porosity} = \frac{N_{\text{pore}}}{N_{\text{pore}} + N_{\text{cross-section}}}$$

The reported porosity and its uncertainty correspond to the mean and standard deviation, respectively, obtained from three cross-sectional images of equal size (2024 μm^2 each).

Conflicts of interest

S. D. Lacey and F. Klunker conducted this research as employees of Huntsman Advanced Materials, which manufactures and markets the CNT-N material.

Data availability

The data supporting the findings of this study are available within the article and its supporting information (SI). Raw data is available from the authors upon reasonable request.

Supplementary information is available. See DOI: https://doi.org/10.1039/d6ta01878e.

Acknowledgements

A. J. Saadun and S. D. Lacey contributed equally to this work. This work was supported by the European Union through the project "SeNSE", which has received funding from the European Union's Horizon 2020 research and innovation program under grant agreement No. 875548. We thank Solvionic for providing the carbonate electrolytes used in the experiments. Andreas Gigl and Larisa Balc (AIT) are acknowledged for their support in electrode manufacturing at pilot scale. Ina Luttenberger and Ernest Kirchmayer (AIT) are acknowledged for their support in pouch cell manufacturing. C. Bozal Ginesta acknowledges funding from the Empa Young Scientist Fellowship.

References

1 T. Hettesheimer, C. Neef, I. R. Inclán, S. Link, T. Schmaltz, F. Schuckert, A. Stephan, M. Stephan, A. Thielmann, L. Weymann, and T. Wicke, *Lithium-Ion Battery Roadmap* -

Industrialization Perspectives toward 2030, Fraunhofer ISI, 2023.
2 W. He, W. Guo, H. Wu, L. Lin, Q. Liu, X. Han, Q. Xie, P. Liu, H. Zheng, L. Wang, X. Yu and D.-L. Peng, *Adv. Mater.*, 2021, **33**, 2005937, DOI: 10.1002/adma.202005937.
3 S. Jiao, J. Wang, Y.-S. Hu, X. Yu and H. Li, *ACS Energy Lett.*, 2023, **8**, 3025, DOI: 10.1021/acsenergylett.3c00563.
4 J. Xiang, Y. Wei, Y. Zhong, Y. Yang, H. Cheng, L. Yuan, H. Xu and Y. Huang, *Adv. Mater.*, 2022, **34**, 2200912, DOI: 10.1002/adma.202200912.
5 S. Li, K. Wang, G. Zhang, S. Li, Y. Xu, X. Zhang, X. Zhang, S. Zheng, X. Sun and Y. Ma, *Adv. Funct. Mater.*, 2022, **32**, 2200796, DOI: 10.1002/adfm.202200796.
6 M. Yamada, T. Watanabe, T. Gunji, J. Wu and F. Matsumoto, *Electrochem*, 2020, **1**, 124, DOI: 10.3390/electrochem1020011.
7 P. Zhu, D. Gastol, J. Marshall, R. Sommerville, V. Goodship and E. Kendrick, *J. Power Sources*, 2021, **485**, 229321, DOI: 10.1016/j.jpowsour.2020.229321.
8 J. F. Baumgärtner, K. V. Kravchyk and M. V. Kovalenko, *Adv. Energy Mater.*, 2025, **15**, 2400499, DOI: 10.1002/aenm.202400499.
9 J. Landesfeind, A. Eldiven and H. A. Gasteiger, *J. Electrochem. Soc.*, 2018, **165**, A1122, DOI: 10.1149/2.0971805jes.
10 G. Bree, D. Horstman and C. T. J. Low, *J. Energy Storage*, 2023, **68**, 107852, DOI: 10.1016/j.est.2023.107852.
11 J. H. Kim, S. Kim, J. H. Han, S. B. Seo, Y. R. Choi, J. Lim and Y. A. Kim, *Carbon Lett.*, 2023, **33**, 325, DOI: 10.1007/s42823-022-00449-0.
12 G. Kucinskis, G. Bajars and J. Kleperis, *J. Power Sources*, 2013, **240**, 66, DOI: 10.1016/j.jpowsour.2013.03.160.
13 F.-Y. Su, Y.-B. He, B. Li, X.-C. Chen, C.-H. You, W. Wei, W. Lv, Q.-H. Yang and F. Kang, *Nano Energy*, 2012, **1**, 429, DOI: 10.1016/j.nanoen.2012.02.004.
14 M. Ko, S. Chae and J. Cho, *ChemElectroChem*, 2015, **2**, 1645, DOI: 10.1002/celc.201500254.
15 X. Gao, F. Wang, S. Gollon and C. Yuan, *J. Electrochem. Energy Convers. Storage*, 2019, **16**, 011009, DOI: 10.1115/1.4040826.
16 Z. Ye, Z. Zou and C. Jiang, *Diam. Relat. Mater.*, 2023, **136**, 109911, DOI: 10.1016/j.diamond.2023.109911.
17 J. Xue, C. Jiang, B. Pan and Z. Zou, *J. Electroanal. Chem.*, 2019, **850**, 113419, DOI: 10.1016/j.jelechem.2019.113419.
18 M. E. Spahr, D. Goers, A. Leone, S. Stallone and E. Grivei, *J. Power Sources*, 2011, **196**, 3404, DOI: 10.1016/j.jpowsour.2010.07.002.
19 M. Wissler, *J. Power Sources*, 2006, **156**, 142, DOI: 10.1016/j.jpowsour.2006.02.064.
20 Huntsman International LLC. *Accelerating the Market Toward Lower Emissions*. https://www.huntsman.com/sustainability/our-solutions/article/14231/accelerating-the-market-toward-lower-emissions (accessed 27 May 2026).
21 Huntsman International LLC. *Construction Underway on Huntsman's 30-Ton Pilot Plant for MIRALON® Carbon Nanotube Materials*. https://www.huntsman.com/news/media-releases/detail/566/construction-underway-on-huntsmans-30-ton-pilot-plant-for (accessed 27 May 2026).
22 H. Yoon, H. Kim, P. Matteini and B. Hwang, *Batteries*, 2022, **8**, 254, DOI: 10.3390/batteries8120254.
23 G. Fugallo, A. Cepellotti, L. Paulatto, M. Lazzeri, N. Marzari and F. Mauri, *Nano Lett.*, 2014, **14**, 6109, DOI: 10.1021/nl502059f.
24 L. Cloos and T. Wetzel, *Energy Technol.*, 2025, **13**, 2402409, DOI: 10.1002/ente.202402409.
25 G. M. Cavalheiro, T. Iriyama, G. J. Nelson, S. Huang and G. Zhang, *J. Electrochem. Energy Convers. Storage*, 2020, **17**, 021101, DOI: 10.1115/1.4045205.
26 D. Andre, M. Meiler, K. Steiner, C. Wimmer, T. Soczka-Guth and D. U. Sauer, *J. Power Sources*, 2011, **196**, 5334, DOI: 10.1016/j.jpowsour.2010.12.102.
27 J.-H. Shim, Y.-M. Kim, M. Park, J. Kim and S. Lee, *ACS Appl. Mater. Interfaces*, 2017, **9**, 18720, DOI: 10.1021/acsami.7b02654.
28 A. Masias, J. Marcicki and W. A. Paxton, *ACS Energy Lett.*, 2021, **6**, 621, DOI: 10.1021/acsenergylett.0c02584.
29 S. Sharifi-Asl, J. Lu, K. Amine and R. Shahbazian-Yassar, *Adv. Energy Mater.*, 2019, **9**, 1900551, DOI: 10.1002/aenm.201900551.